Coordination of robust single cell rhythms in the *Arabidopsis* circadian clock via spatial waves of gene expression

Peter D. Gould[1+], Mirela Domijan[2,3+], Mark Greenwood[1,2,4], Isao T. Tokuda[5], Hannah Rees[1], Laszlo Kozma-Bognar[6], Anthony J.W. Hall[1,7*], James C.W. Locke[2,4,8*]

[1]Institute of Integrative Biology, University of Liverpool, Crown Street, Liverpool, L69 7ZB, UK

[2]Sainsbury Laboratory, University of Cambridge, Bateman Street, Cambridge, CB2 1LR, UK

[3]Department of Mathematical Sciences, University of Liverpool, Peach Street, Liverpool, L69 7ZL

[4]Department of Biochemistry, University of Cambridge, 80 Tennis Court Road, Cambridge, CB2 1QW, UK

[5]Department of Mechanical Engineering, Ritsumeikan University, Noji-higashi, Kusatsu, 525-8577, Japan

[6]Biological Research Centre, Hungarian Academy of Sciences, 6726 Szeged, Hungary

[7]Earlham Institute, Norwich Research Park, Norwich, NR4 7UH, UK

[8]Microsoft Research, 21 Station Road, Cambridge, CB1 2FB, UK

*Email: james.locke@slcu.cam.ac.uk or anthony.hall@earlham.ac.uk

+Equal Contribution

The *Arabidopsis* circadian clock orchestrates gene regulation across the day/night cycle. Although a multiple feedback loop circuit has been shown to generate the 24h rhythm, it remains unclear how robust the clock is in individual cells, or how clock timing is coordinated across the plant. Here we examine clock activity at the single cell level across *Arabidopsis* seedlings over several days. Our data reveal robust single cell oscillations, albeit desynchronised. In particular, we observe two waves of clock activity; one going down, and one up the root. We also find evidence of cell-to-cell coupling of the clock, especially in the root tip. A simple model shows that cell-to-cell coupling and our measured period differences between cells can generate the observed waves. Our results reveal the spatial structure of the plant circadian clock and suggest that unlike the centralised mammalian clock, the clock has multiple points of coordination in *Arabidopsis*.

30   **Introduction**

31

32   The circadian clock controls gene expression throughout the day and night in most

33   organisms, from single cell photosynthetic bacteria to mammals (Bell-Pedersen et al.,

34   2005). In many cases a core circuit that generates this rhythm has been elucidated and

35   been shown to oscillate in single cells. In multi-cellular organisms these single cell

36   rhythms must be integrated to allow a coordinated response to the environment.

37   Mammals achieve this by driving oscillations in peripheral tissues from a central

38   pacemaker in the brain, the suprachiasmatic nucleus (SCN) (Pando, Morse,

39   Cermakian, & Sassone-Corsi, 2002; Reppert & Weaver, 2002).

40   The *Arabidopsis* circadian clock generates a 24h rhythm in multiple key processes,

41   including stomata opening, photosynthesis, and hypocotyl elongation (Hsu & Harmer,

42   2014). A hierarchical structure for the plant clock has recently been proposed, similar

43   to that for the mammalian clock, where the shoot clock drives the rhythms in the

44   leaves and roots (Takahashi, Hirata, Aihara, & Mas, 2015). However, there are further

45   tissue dependent differences that must be explained. For example, experiments using

46   a luciferase reporter for clock activity have shown waves of clock gene expression in

47   leaves (Fukuda, Nakamichi, Hisatsune, Murase, & Mizuno, 2007; Wenden, Toner,

48   Hodge, Grima, & Millar, 2012), as well as striped expression patterns in roots

49   (Fukuda, Ukai, & Oyama, 2012).

50   Beyond the coordination of plant rhythms, how robust the circadian clock is in

51   individual cells across the plant is also unclear. Through integration of data from

52   whole plant studies, a genetic circuit consisting of multiple coupled feedback loops

53   has been proposed to generate the 24h rhythm (Fogelmark & Troein, 2014; Pokhilko

54   et al., 2012). Simulations of this network display stable oscillations (Figure 1a),

55   although experimental measurements of clock rhythms under constant conditions

56   often display damped rhythms (Figure 1b) (Gould et al., 2013; Locke et al., 2005,

57   2006; Salomé & McClung, 2005). This damping could be due to the clock circuit in

58   individual cells losing rhythmicity (top, Figure 1c), or to cells desynchronising due to

59   different intrinsic periods or phases (Guerriero et al., 2012; Komin, Murza,

60   Hernández-García, & Toral, 2010) (bottom, Figure 1c), or cells desynchronising due

61   to stochasticity in clock activity (Guerriero et al., 2012). Previous studies have

62   attempted to measure the clock in plants at single-cell resolution; however, these have

63   been confounded by poor temporal/spatial resolution and short time series (Takahashi

64   et al., 2015; Yakir et al., 2011).

65   Here, we examine the dynamics of the *Arabidopsis* clock across the whole plant at the

66   single cell level over several days. Our results reveal that damping of rhythms is

67   mainly due to desynchronisation of oscillating single cells with different periods, and

68   not due to noise in gene expression or lack of robustness. We observe two waves of

69   clock gene expression, one up and one down the root, which cause the most

70   desynchronisation. From our single cell data, we are able to estimate the coupling

71   strength between cells, and find evidence of coupling, especially strong in the root tip.

72   A simple model suggests that our observed period differences, plus cell-to-cell

73   coupling, can generate the observed waves in clock gene expression. Thus, our data

74   has revealed both the structure and robustness of the plant circadian clock system.

75

76   **Results**

77   To analyse the dynamics of the plant clock at the single cell level, we constructed

78   reporter lines that allowed us to quantitatively measure the nuclear level of the core

3

79   clock protein CIRCADIAN CLOCK ASSOCIATED 1 (CCA1) (Wang & Tobin,

80   1998). These reporter lines contained a CCA1-YFP protein fusion construct driven by

81   the *CCA1* promoter in a *cca1-11* mutant background. They also contained a

82   35S::H2B-RFP nuclear marker to enable automatic detection of individual nuclei

83   (Federici, Dupuy, Laplaze, Heisler, & Haseloff, 2012). By screening the clock

84   phenotypes of multiple reporter lines we ensured that our reporter construct was

85   functional and rescued the period phenotype of the *cca1-11* mutant (Figure 1-figure

86   supplement 1). We took forward both a rescued wild-type period (WT) and a long

87   period (CCA1-long) reporter line for further analysis.

88

89   We carried out time-lapse movies of *Arabidopsis* seedlings using a custom developed

90   time-lapse confocal microscope setup (Figure 1-figure supplement 2). In order to

91   examine the intrinsic behavior of the clock we first entrained the seedlings to 12:12h

92   light/dark cycles before examining the clock under constant conditions (constant blue

93   light (30 μmol m^{-2} s^{-1}) and temperature (22 °C)), as standard in circadian research.

94   Our method allowed us to track and extract fluorescence values from the same

95   individual nuclei over several days (Figure 1d, e). We first examined the average

96   CCA1-YFP nuclear fluorescence signal from regions of the hypocotyl, cotyledon and

97   roots (Figure 1f, g). We observed a robust oscillation in the cotyledon (red line,

98   Figure 1g) and hypocotyl (blue line, Figure 1g), although with slight damping to the

99   amplitude. In the top part of the root we observed strong damping of the circadian

100   rhythm (black line, Figure 1g), although surprisingly the oscillations recovered

101   somewhat in the root tip (grey line, Figure 1g). Three repeat plants showed similar

102   behavior (Figure 1-figure supplement 3). We also observed similar behavior in our

4

103   CCA1-long reporter line (Figure 1-figure supplement 4), showing that our results

104   remain true across a range of clock activity.

105

106   To determine what the underlying cause of the damping in different tissues was we

107   examined the clock rhythm in thousands of individual cells (Figure 1h, Figure 1-

108   figure supplement 3b, 4b, 5). Oscillations could be observed in all tissues, with most

109   cells displaying circadian oscillations (Figure 1, Figure 1-source data 1, 2). It is clear

110   from the traces that the strong damping in the mean levels in the root is not caused by

111   individual oscillators losing rhythmicity (Figure 1h). We then examined the

112   synchronicity and robustness of these rhythms in more detail. The hypocotyl and

113   cotyledon were the most synchronised, with the amplitude of the mean trace nearly

114   equaling the median amplitude of the individual cell lineages (Figure 2a, Figure 2-

115   figure supplement 1, 2). The hypocotyl and cotyledon rhythms also exhibited low

116   period variability both within and between cell lineages, indicating a high level of

117   robustness (Figure 2b, Figure 2-figure supplement 1b, 2b). However, the root

118   displayed significant desynchronisation, with the amplitude of the mean trace lower

119   than the median amplitude of the individual cell lineages (Figure 2a, Figure 2-figure

120   supplement 1a, 2a), with higher variability in period within and between single cell

121   lineages (Figure 2b and Figure 2-figure supplement 1b, 2b).

122

123   We next asked whether the damping of amplitude in the mean rhythm is caused by

124   noise in gene expression, as proposed by previous stochastic modelling (Guerriero et

125   al., 2012). Simulations of the stochastic model of the *Arabidopsis* gene network

126   (Guerriero et al., 2012) display greater desynchronisation as the system size,

127   effectively the simulated number of molecules in the cell, is reduced (Figure 2c-e).

128   The lower the molecule number, the more desynchronisation at the single cell level,

129   and the more damping of the mean expression (red line, Figure 2c). To explore this

130   further, we simulated the model for a range of system sizes (Figure 2c) and examined

131   the synchronicity and robustness of the simulations (Figure 2d, e). Previously the

132   system size was estimated to be of order 100 molecules per cell (bottom panel, Figure

133   2c) in order for the desynchronisation observed in whole plant measurements to be

134   explained solely by noise (Guerriero et al., 2012). We compared the level of

135   desynchronisation and noise from simulations of this model to our experimentally

136   measured single cell rhythms. The single cell rhythms that we detect in the hypocotyl

137   and cotyledon are more robust than a system size of 100, and in fact behave closer to

138   a system size of 1000 (top panel, Figure 2c). The level of desynchronisation observed

139   in the root and root tip, however, behave more like a simulated system size of 100

140   (Figure 2b, c). Similar CCA1-YFP expression levels are observed across the plant

141   (Figure 2f, g), so it is unlikely that this lack of robustness is due solely to a change of

142   total molecule number for the clock system in different parts of the plant. In fact the

143   amplitude and expression levels of the single cell oscillations in the root tip are high

144   compared to other sections across the plant (Figure 2f, g and Figure 2-figure

145   supplement 1a, c-d, 2a, c-d).

146

147   If the damping in the root is not due to noise in gene expression, or individual cells

148   losing rhythmicity, what does cause it? The measured variable and desynchronous

149   rhythms in the root suggest that the clock could be behaving differently in different

150   parts of the root. To test this possibility we plotted the period of the individual cell

151   oscillations across the plant (Figure 3a, b and Figure 2-figure supplement 1e, f and 2e,

152   f). We observed surprising spatial structure to the clock in the root. The upper

153   sections of the root displayed longer periods than the rest of the plant, as reported

154   previously for the whole root (James et al., 2008). However, we observed very fast

155   rhythms in the root tip (Figure 3a, b), which is also the section with very high

156   expression rhythms (Figure 2f, g). Although we do not observe evidence of phase

157   resetting in the root tip, as proposed in an earlier luciferase study (Fukuda et al.,

158   2012), this could be due to our different growth conditions and stage of plant

159   development. A repeat plant showed similar results (Figure 2-figure supplement 1c-f),

160   as did the CCA1-long reporter line (Figure 2-figure supplement 2c-f). Each section of

161   the plant can be made up of multiple cell types. So, we next tested whether the

162   rhythms have any spatial structure in the *z* direction, which would suggest that

163   different cell types have different period rhythms. Plots of period in the *z* direction in

164   each section do not reveal any discernable pattern, including in the root, where cells

165   are organised radially (Figure 3c, d). This suggests that the differences in rhythms we

166   observe are not restricted to a specific cell type.

167

168   To further understand the spatial structure of the clock, we examined montages of

169   clock gene expression (Figure 3e; Figure 2-figure supplement 1g; Videos 1-3) and

170   timing of peaks of expression (Figure 3f-h) across the plant. The clock peaks earlier in

171   the hypocotyl than in the cotyledon (Figure 3f-h), and the phase of the rhythm is also

172   tightest in the hypocotyl, where the phase varies by a standard deviation of 1.47h in

173   the first peak and 3.09h in last peak (Figure 3g), with more desynchronisation in the

174   cotyledon (Figure 3f). From the top of the root the phase of the clock is shifted to later

175   in the day as you go down the root (Figure 3h). However, from the root tip the phase

176   of the clock is shifted to later in the day as you go up. This generates two waves in the

177   montages of clock gene expression, one going up and one going down the root

178   (Figure 3e; Video 1; Figure 2-figure supplement 1g, 2g). Thus, the damped mean

179   rhythm of clock activity we observed in the root (Figure 1g) is caused by the

180   averaging of these two waves of gene expression. We observed qualitatively similar

181   waves in two clock luciferase reporter lines, PSEUDO-RESPONSE REGULATOR

182   9:LUC (Salomé & McClung, 2005) (Figure 3i; Video 4) and CCA1:LUC (Figure 3-

183   figure supplement 1), showing that our results are a general property of the clock.

184

185   The coherent waves of gene expression suggested that the plant clock signal could be

186   coupled. To estimate this coupling, we calculated the order parameter (Kuramoto,

187   1984) from our single cell data and estimated the coupling strength based on a

188   technique developed for mammalian circadian cells (Rougemont & Naef, 2007). We

189   observed signs of coupling across the plant, with the strongest evidence for coupling

190   in the root tip, where the order parameter actually increased with time (Figure 3j and

191   Figure 2-figure supplement 2-4). Interestingly this occurred where cell density was

192   highest, as observed in cultured SCN cells (Aton, Colwell, Harmar, Waschek, &

193   Herzog, 2005). To investigate the mechanism for the waves of clock gene expression

194   in the root we developed a simple mathematical model where the cells are described

195   by coupled phase oscillators with different periods, as informed by the data (Figure

196   3k). The periods of the clock in the model were faster in the shoot and root tip than

197   the rest of the root, as measured experimentally. This simple model can generate

198   waves of gene expression up and down the root that produce a bow wave in the space-

199   time plot (Figure 3k), similar to that observed experimentally (Figure 3h, i).

200

201

202

203 **Discussion**

204

205   Our single cell measurements have revealed tissue specific differences in the phases

206   and robustness of the clock in *Arabidopsis*. These differences are not restricted to one

207   cell type, as similar periods are observed in the *z* dimension through the plant (Figure

208   3c, d), suggesting that cells are instead responding to information based on their

209   longitudinal position. The observed robust rhythms in the hypocotyl that peak before

210   the cotyledon and roots are in line with a proposed hierarchical structure for the plant

211   clock, where the shoot clock drives the rhythms in the leaves and roots (Takahashi et

212   al., 2015). However, our results suggest that the structure of the plant clock is more

213   complicated, as this hierarchical model does not explain the observed short period

214   oscillations in the root tip. Our results support a more decentralised model of clock

215   coordination in plants (Endo, 2016; Endo, Shimizu, Nohales, Araki, & Kay, 2014).

216

217   Earlier studies of the clock argue either that the clock is uncoupled (Thain, Hall, &

218   Millar, 2000; Yakir et al., 2011), or weakly, but detectably, coupled (Fukuda et al.,

219   2007, 2012; James et al., 2008; Takahashi et al., 2015; Wenden et al., 2012). Our

220   single cell approach is consistent with weak coupling across the whole plant but

221   reveals regions with strong local coupling between cells, especially in the root tip,

222   which is sufficient to drive an increase in synchrony with time. Our modelling shows

223   that this coupling together with the observed period differences is sufficient to

224   replicate the decentralised spatial structure of the clock that we observe

225   experimentally.

226

227   Decentralised coordination could create flexibility and allow parts of the plant to

228   respond differentially to environmental perturbations. There is already evidence that

229   the root clock may respond differently to light (Bordage, Sullivan, Laird, Millar, &

230   Nimmo, 2016), and that the vasculature and epidermal clock regulate distinct

231   physiological processes (Shimizu et al., 2015). It has been recently shown that

232   initiation of lateral roots triggers the resetting of the clock in the emerging lateral root

233   (Voß et al., 2015). In the case of lateral roots auxin is proposed to be involved in

234   resetting the clock (Voß et al., 2015). An important next step will be to investigate

235   what the coupling signal is for the plant circadian clock (Covington & Harmer, 2007;

236   Dalchau et al., 2011; Haydon, Mielczarek, Robertson, Hubbard, & Webb, 2013).

237

238   **References**

239   Aton, S. J., Colwell, C. S., Harmar, A. J., Waschek, J., & Herzog, E. D. (2005).

240   Vasoactive intestinal polypeptide mediates circadian rhythmicity and synchrony

241   in mammalian clock neurons. *Nature Neuroscience*, *8*(4), 476.

242   https://doi.org/10.1038/nn1419

243   Bell-Pedersen, D., Cassone, V. M., Earnest, D. J., Golden, S. S., Hardin, P. E.,

244   Thomas, T. L., & Zoran, M. J. (2005). Circadian rhythms from multiple

245   oscillators: lessons from diverse organisms. *Nature Reviews Genetics*, *6*(7), 544–

246   556. https://doi.org/10.1038/nrg1633

247   Bordage, S., Sullivan, S., Laird, J., Millar, A. J., & Nimmo, H. G. (2016). Organ

248   specificity in the plant circadian system is explained by different light inputs to

249   the shoot and root clocks. *The New Phytologist*, *212*(1), 136–49.

250   https://doi.org/10.1111/nph.14024

251   Costa, M. J., Finkenstädt, B., Roche, V., Lévi, F., Gould, P. D., Foreman, J., … Rand,

252   D. A. (2013). Inference on periodicity of circadian time series. *Biostatistics*,

253   *14*(4), 792–806. https://doi.org/10.1093/biostatistics/kxt020

254 Covington, M. F., & Harmer, S. L. (2007). The circadian clock regulates auxin

255   signaling and responses in Arabidopsis. *PLoS Biology*, *5*(8), e222.

256   https://doi.org/10.1371/journal.pbio.0050222

257 Dalchau, N., Baek, S. J., Briggs, H. M., Robertson, F. C., Dodd, A. N., Gardner, M.

258   J., … Webb, A. A. R. (2011). The circadian oscillator gene GIGANTEA

259   mediates a long-term response of the Arabidopsis thaliana circadian clock to

260   sucrose. *Proceedings of the National Academy of Sciences of the United States of*

261   *America*, *108*(12), 5104–9. https://doi.org/10.1073/pnas.1015452108

262 Edwards, K. D., Akman, O. E., Knox, K., Lumsden, P. J., Thomson, A. W., Brown, P.

263   E., … Millar, A. J. (2010). Quantitative analysis of regulatory flexibility under

264   changing environmental conditions. *Molecular Systems Biology*, *6*(1), 424.

265   https://doi.org/10.1038/msb.2010.81

266 Endo, M. (2016). Tissue-specific circadian clocks in plants. *Current Opinion in Plant*

267   *Biology*, *29*, 44–49. https://doi.org/10.1016/j.pbi.2015.11.003

268 Endo, M., Shimizu, H., Nohales, M. A., Araki, T., & Kay, S. A. (2014). Tissue-

269   specific clocks in Arabidopsis show asymmetric coupling. *Nature*, *515*, 419–422.

270 Federici, F., Dupuy, L., Laplaze, L., Heisler, M., & Haseloff, J. (2012). Integrated

271   genetic and computation methods for in planta cytometry. *Nature Methods*, *9*(5),

272   483–485. https://doi.org/10.1038/nmeth.1940

273 Fogelmark, K., & Troein, C. (2014). Rethinking transcriptional activation in the

274   Arabidopsis circadian clock. *PLoS Computational Biology*, *10*(7), e1003705.

275   https://doi.org/10.1371/journal.pcbi.1003705

276 Fukuda, H., Nakamichi, N., Hisatsune, M., Murase, H., & Mizuno, T. (2007).

277   Synchronization of Plant Circadian Oscillators with a Phase Delay Effect of the

11

278   Vein Network. *Physical Review Letters*, *99*(9), 98102.

279   https://doi.org/10.1103/PhysRevLett.99.098102

280   Fukuda, H., Ukai, K., & Oyama, T. (2012). Self-arrangement of cellular circadian

281   rhythms through phase-resetting in plant roots. *Physical Review E*, *86*(4), 41917.

282   https://doi.org/10.1103/PhysRevE.86.041917

283   Gillespie, D. T. (1977). Exact stochastic simulation of coupled chemical reactions.

284   *The Journal of Physical Chemistry*, *81*(25), 2340–2361.

285   https://doi.org/10.1021/j100540a008

286   Gould, P. D., Diaz, P., Hogben, C., Kusakina, J., Salem, R., Hartwell, J., & Hall, A.

287   (2009). Delayed fluorescence as a universal tool for the measurement of

288   circadian rhythms in higher plants. *The Plant Journal*, *58*, 893–901.

289   Gould, P. D., Ugarte, N., Domijan, M., Costa, M., Foreman, J., Macgregor, D., …

290   Hall, A. J. W. (2013). Network balance via CRY signalling controls the

291   Arabidopsis circadian clock over ambient temperatures. *Molecular Systems*

292   *Biology*, *9*, 650. https://doi.org/10.1038/msb.2013.7

293   Guerriero, M. L., Pokhilko, A., Fernández, A. P., Halliday, K. J., Millar, A. J., &

294   Hillston, J. (2012). Stochastic properties of the plant circadian clock. *Journal of*

295   *the Royal Society, Interface*, *9*(69), 744–756.

296   https://doi.org/10.1098/rsif.2011.0378

297   Hall, A., Bastow, R. M., Davis, S. J., Hanano, S., McWatters, H. G., Hibberd, V., …

298   Millar, A. J. (2003). The TIME FOR COFFEE gene maintains the amplitude and

299   timing of Arabidopsis circadian clocks. *The Plant Cell*, *15*(11), 2719–29.

300   https://doi.org/10.1105/tpc.013730

301   Haydon, M. J., Mielczarek, O., Robertson, F. C., Hubbard, K. E., & Webb, A. A. R.

302   (2013). Photosynthetic entrainment of the Arabidopsis thaliana circadian clock.

303   *Nature*, *502*(7473), 689–92. https://doi.org/10.1038/nature12603

304   Hsu, P. Y., & Harmer, S. L. (2014). Wheels within wheels: the plant circadian system.

305   *Trends in Plant Science*, *19*(4), 240–9.

306   https://doi.org/10.1016/j.tplants.2013.11.007

307   James, A. B., Monreal, J. A., Nimmo, G. A., Kelly, C. L., Herzyk, P., Jenkins, G. I.,

308   & Nimmo, H. G. (2008). The circadian clock in Arabidopsis roots is a simplified

309   slave version of the clock in shoots. *Science*, *322*(5909), 1832–5.

310   https://doi.org/10.1126/science.1161403

311   Johnson, M., & Frasier, S. (1985). Nonlinear least squares analysis. *Methods*

312   *Enzymol.*, *117*, 301–342.

313   Kellogg, R. A., & Tay, S. (2015). Noise facilitates transcriptional control under

314   dynamic inputs. *Cell*, *160*(3), 381–92. https://doi.org/10.1016/j.cell.2015.01.013

315   Komin, N., Murza, A. C., Hernández-García, E., & Toral, R. (2010). Synchronization

316   and entrainment of coupled circadian oscillators. *Interface Focus*, *1*(1).

317   Kuramoto, Y. (1984). *Chemical Oscillations, Waves, and Turbulence* (Vol. 19).

318   Berlin, Heidelberg: Springer Berlin Heidelberg. https://doi.org/10.1007/978-3-

319   642-69689-3

320   Litthauer, S., Battle, M. W., Lawson, T., & Jones, M. A. (2015). Phototropins

321   maintain robust circadian oscillation of PSII operating efficiency under blue

322   light. *The Plant Journal*, *83*(6), 1034–1045. https://doi.org/10.1111/tpj.12947

323   Locke, J. C. W., Kozma-Bognár, L., Gould, P. D., Fehér, B., Kevei, E., Nagy, F., …

324   Millar, A. J. (2006). Experimental validation of a predicted feedback loop in the

325   multi-oscillator clock of Arabidopsis thaliana. *Molecular Systems Biology*, *2*, 59.

326   https://doi.org/10.1038/msb4100102

327   Locke, J. C. W., Southern, M. M., Kozma-Bognár, L., Hibberd, V., Brown, P. E.,

328   Turner, M. S., & Millar, A. J. (2005). Extension of a genetic network model by

329   iterative experimentation and mathematical analysis. *Molecular Systems Biology*,

330   *1*, 2005.0013. https://doi.org/10.1038/msb4100018

331   Moore, A., Zielinski, T., & Millar, A. J. (2014). Online period estimation and

332   determination of rhythmicity in circadian data, using the BioDare data

333   infrastructure. *Methods in Molecular Biology*, *1158*, 13–44.

334   https://doi.org/10.1007/978-1-4939-0700-7_2

335   Pando, M. P., Morse, D., Cermakian, N., & Sassone-Corsi, P. (2002). Phenotypic

336   rescue of a peripheral clock genetic defect via SCN hierarchical dominance. *Cell*,

337   *110*(1), 107–17.

338   Pfeiffer, A., Kunkel, T., Hiltbrunner, A., Neuhaus, G., Wolf, I., Speth, V., … Schäfer,

339   E. (2009). A cell-free system for light-dependent nuclear import of phytochrome.

340   *The Plant Journal*, *57*(4), 680–689. https://doi.org/10.1111/j.1365-

341   313X.2008.03721.x

342   Pokhilko, A., Fernández, A. P., Edwards, K. D., Southern, M. M., Halliday, K. J., &

343   Millar, A. J. (2012). The clock gene circuit in Arabidopsis includes a

344   repressilator with additional feedback loops. *Molecular Systems Biology*, *8*(1),

345   574. https://doi.org/10.1038/msb.2012.6

346   Reppert, S. M., & Weaver, D. R. (2002). Coordination of circadian timing in

347   mammals. *Nature*, *418*(6901), 935–941. https://doi.org/10.1038/nature00965

348   Rougemont, J., & Naef, F. (2007). Dynamical signatures of cellular fluctuations and

349   oscillator stability in peripheral circadian clocks. *Molecular Systems Biology*, *3*,

350   93. https://doi.org/10.1038/msb4100130

351   Salomé, P. A., & McClung, C. R. (2005). PSEUDO-RESPONSE REGULATOR 7

352   and 9 are partially redundant genes essential for the temperature responsiveness

353 of the Arabidopsis circadian clock. *The Plant Cell*, *17*(3), 791–803.

354 https://doi.org/10.1105/tpc.104.029504

355 Shimizu, H., Katayama, K., Koto, T., Torii, K., Araki, T., & Endo, M. (2015).

356 Decentralized circadian clocks process thermal and photoperiodic cues in

357 specific tissues. *Nature Plants*, *1*(11), 15163.

358 https://doi.org/10.1038/nplants.2015.163

359 Straume, M., Frasier-Cadoret, S. G., & Johnson, M. L. (2002). Least-Squares

360 Analysis of Fluorescence Data. In *Topics in Fluorescence Spectroscopy* (pp.

361 177–240). Boston: Kluwer Academic Publishers. https://doi.org/10.1007/0-306-

362 47058-6_4

363 Takahashi, N., Hirata, Y., Aihara, K., & Mas, P. (2015). A Hierarchical Multi-

364 oscillator Network Orchestrates the Arabidopsis Circadian System. *Cell*, *163*(1),

365 148–159. https://doi.org/10.1016/j.cell.2015.08.062

366 Thain, S. C., Hall, A., & Millar, A. J. (2000). Functional independence of circadian

367 clocks that regulate plant gene expression. *Current Biology*, *10*(16), 951–6.

368 Voß, U., Wilson, M. H., Kenobi, K., Gould, P. D., Robertson, F. C., Peer, W. A., …

369 Bennett, M. J. (2015). The circadian clock rephases during lateral root organ

370 initiation in Arabidopsis thaliana. *Nature Communications*, *6*, 7641.

371 https://doi.org/10.1038/ncomms8641

372 Wang, Z. Y., & Tobin, E. M. (1998). Constitutive expression of the CIRCADIAN

373 CLOCK ASSOCIATED 1 (CCA1) gene disrupts circadian rhythms and

374 suppresses its own expression. *Cell*, *93*(7), 1207–17.

375 Wenden, B., Toner, D. L. K., Hodge, S. K., Grima, R., & Millar, A. J. (2012).

376 Spontaneous spatiotemporal waves of gene expression from biological clocks in

377 the leaf. *Proceedings of the National Academy of Sciences of the United States of*

378   *America*, *109*(17), 6757–6762. https://doi.org/10.1073/pnas.1118814109

379   Yakir, E., Hassidim, M., Melamed-Book, N., Hilman, D., Kron, I., & Green, R. M.

380   (2011). Cell autonomous and cell-type specific circadian rhythms in Arabidopsis.

381   *The Plant Journal*, *68*(3), 520–531. https://doi.org/10.1111/j.1365-

382   313X.2011.04707.x

383

Acknowledgements

392

Contributions

394   A.J.W.H. and J.C.W.L. designed the research. P.D.G. developed the time-lapse

395   microscopy platform and carried out the microscopy and delayed fluorescence

396   imaging. M.D. carried out the mathematical modelling and statistics. M.G. carried out

397   the luciferase imaging and analysis. L.K. completed the cloning. P.D.G., H.R., M.D.,

398   M.G. and I.T. carried out analysis of single cell data. All authors contributed to the

399   writing of the manuscript.

400

Competing interests

402   The authors declare no competing financial interests.

16

403   **Figures**

404

405

406

407

408

409

410

411

412

413

414

415

416

417

418

419   **Figure 1. Quantitative time-lapse microscopy reveals single cell clock dynamics**

420   **across the plant. a**, Current models of the clock (Pokhilko et al., 2012) predict

421   undamped oscillations. **b**, CCA1:LUC bulk averaged over multiple seedlings shows

422   damping clock oscillations (mean ± s.e.m.; $n = 32$ seedlings). **c**, The reason for

423   damping could be due to damping rhythms in individual cells (top) or due to

424   desynchronisation between cells (bottom). **d**, Images show a representative nuclei

425   from the cotyledon of a *cca1-11* CCA1::CCA1-YFP; 35S::H2B-RFP seedling that

426   had been grown in LD cycles before being released into continuous light free running

17
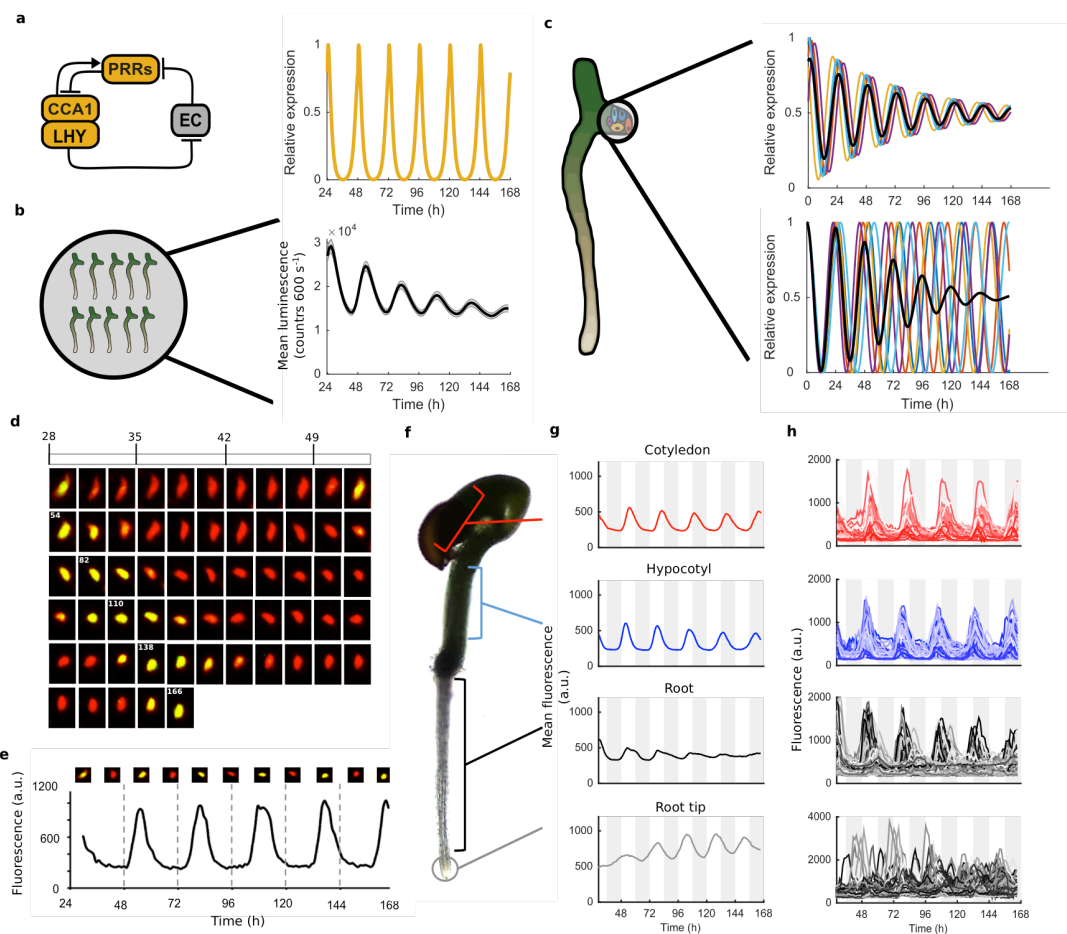
427   conditions for several days. The red channel represents when H2B fluoresce and the

428   yellow CCA1. Times of peak expression are indicated on images. **e**, Expression levels

429   of CCA1-YFP from the representative nuclei shown in (**d**). Images of the nuclei are

430   also shown for the peaks and troughs in the CCA1-YFP oscillation. **f**, Representative

431   seedling identifying the different sections imaged. **g**, Mean traces of single cell

432   CCA1-YFP for over 5 days of constant light in different regions of the plant showing

433   damping rhythms in the root, but not the root tip. **h**, CCA1-YFP traces from

434   individual cell in each section for the same 5 days.

435

436

437

438

439

440

441

442

443

444

445

446

447

448

449

450

451

452

453

454

455

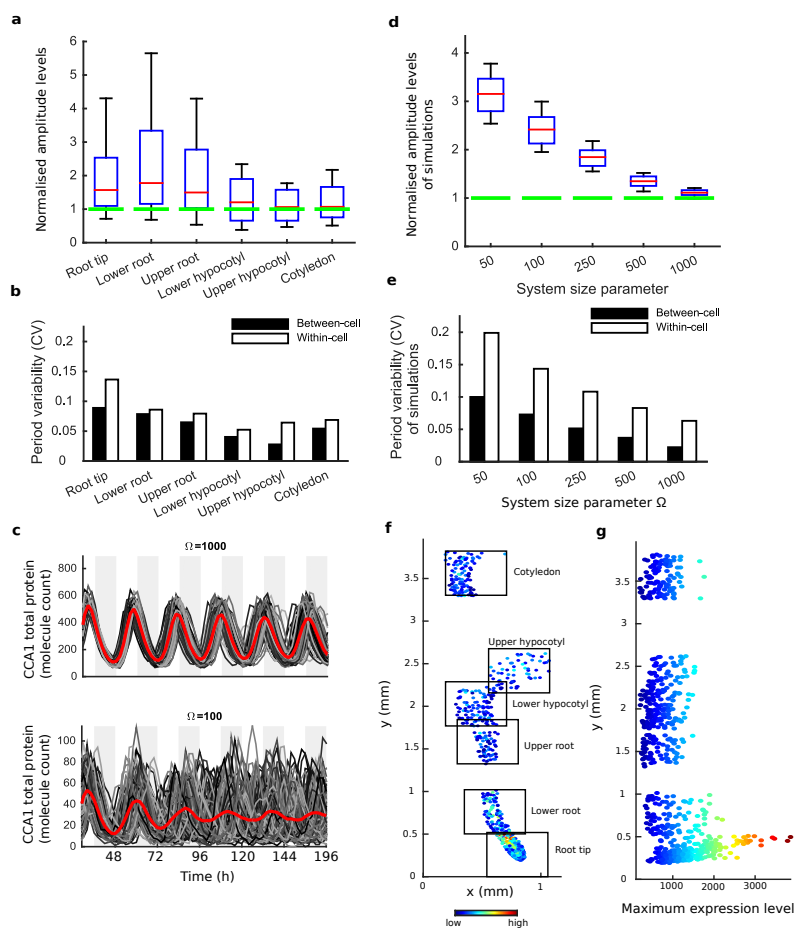456

457

458

459

460

461

462

463

464

465

466 **Figure 2. Single cell analysis reveals tissue level differences in robustness of the**

467 **clock. a**, Rhythmic cell amplitudes in the imaged sections normalised to the

468 amplitude of the mean trace (green line). For root tip, $n = 242$; lower root, $n = 83$;

469 upper root, $n = 46$; lower hypocotyl, $n = 114$; upper hypocotyl, $n = 53$; cotyledon, $n =$

470 103. Whiskers represent 9th and 91st percentile, n the number of cells. **b**, Between-cell

471 and within-cell period variability in each imaged section. **c**, Stochastic model CCA1

472 total molecule count for $\Omega = 1000$ (top) and $\Omega = 100$ for 100 (bottom) simulated runs

473 (grey) plotted from 29h to 168h in constant light (comparable to the data in Figure 1).

474 Means of all simulated runs are shown in red. Ω represents the system size. **d**,

475 Rhythmic simulated run amplitudes for different system sizes (Ω) normalised to the

476 mean simulation (green line). **e**, Between and within cell variability of each

19

477   simulation with different scaling factor. **f**, Scatterplot of the rhythmic cells in all

478   imaged plant sections stitched together. Colour indicates the oscillation amplitude. **g**,

479   Scatterplot of the amplitude values vs. longitudinal position on the plant measured

480   from the root tip. Colour legend is the same as (**f**).

481

482

483

484

485

486

487

488

489

490

491

492

493

494

495

496

497

498
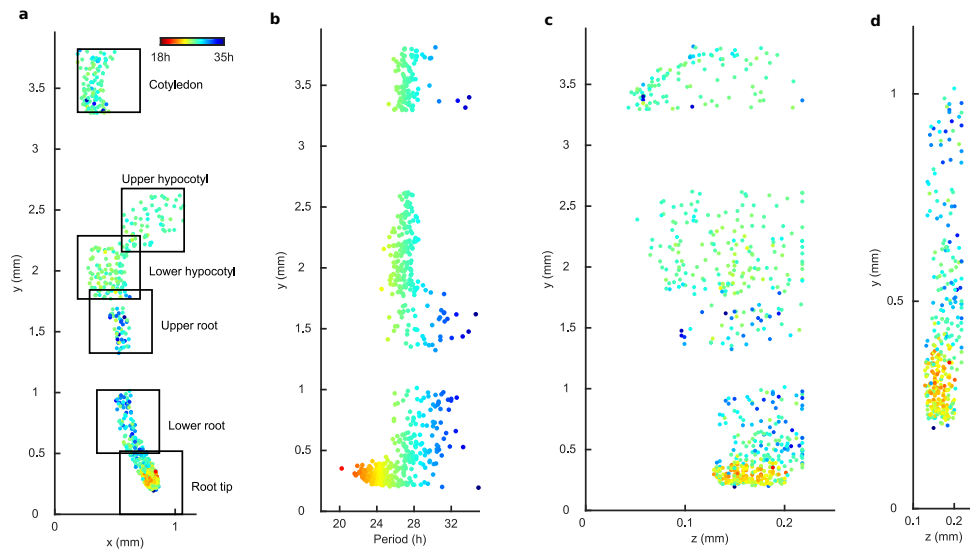
499

500

20

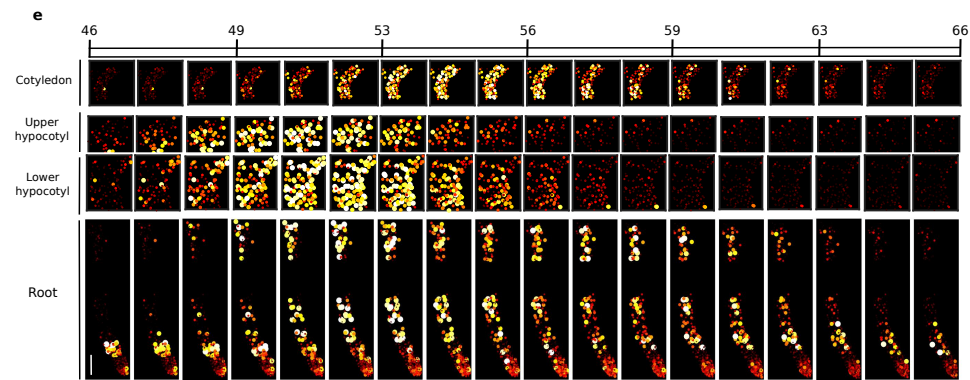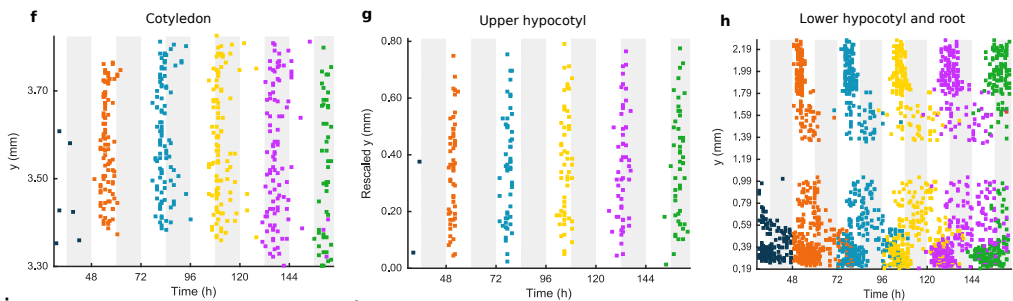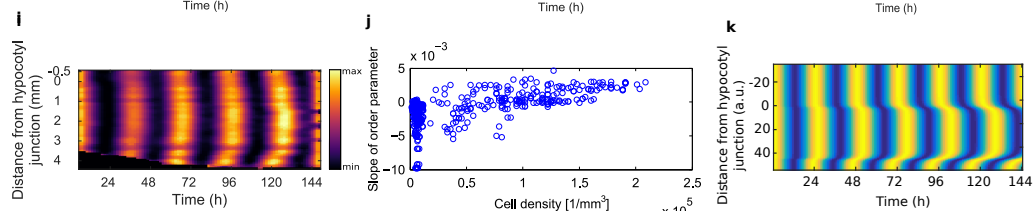**Figure 3. Single cell period differences and cell-to-cell coupling generate spatial waves of clock gene expression. a**, Scatterplot of the rhythmic cells in all imaged plant sections stitched together in *x-y* direction. Colour indicates the oscillation

526   period. **b**, Period values vs. longitudinal position on the plant measured from the root

527   tip. Colour legend is the same as (**a**). **c**, **d**, Scatterplot in the *y-z* direction of rhythmic

528   cells in all imaged plant sections (**c**) or in the root and root tip sections only (**d**).

529   Colour legend is the same as (**a**). **e**, Montage of the normalised expression of

530   rhythmic cells from the root (bottom panel, first image taken after 46.1h in LL), lower

531   hypocotyl (taken after 46.6h in LL), upper hypocotyl (taken after 46.7h) and

532   cotyledon (top panel, taken after 46.9h in LL). Each frame is approximately 1.1h

533   apart. Scale bar represents 0.25 mm. **f-h**, Space-time plots of peak times of rhythmic

534   cells across sections: cotyledon (**f**) upper hypocotyl (**g**), lower hypocotyl and root (all

535   sections) (**h**). **i**, Representative space-time plot of normalised PRR9:LUC expression

536   across longitudinal sections of a seedling (N = 2, *n* = 7). *N* represents the number of

537   independent experiments, *n* the total number of individual seedlings. **j**, Slopes of the

538   order parameter are plotted against cell densities. A positive slope indicates that the

539   level of synchrony increases in time due to cell-cell interactions. **k**, Space-time plot of

540   simulated total normalized *CCA1* expression across longitudinal sections of the

541   seedling.

542

543

544

545

546

547

548

549 **Methods**

550 **Constructs.** The CCA1::CCA1-YFP was constructed as follows: The coding region

551 of *CCA1* was amplified from *Arabidopsis* (Ws) genomic DNA using the primer pair

552 CCA1_CDS_Fwd (5'-AAAGGATCCATGGAGACAAATTCGTCTGGA-3') and

553 CCA1_CDS_Rev (5'-ATACCCGGGTGTGGAAGCTTGAGTTTCCAA-3'). The

554 *CCA1* promoter region was amplified from *Arabidopsis* (Ws) genomic DNA using the

555 primer pair CCA1_prom_Fwd (5'-

556 AAAGAATTCATTTAGTCTTCTACCCTTCATGC-3') and the CCA1_prom_Rev

557 (5'-ATAGGATCCCACTAAGCTCCTCTACACAACTTC-3'). Unique restriction

558 sites were designed at the ends of the amplicons to facilitate cloning. The fragment of

559 *CCA1* coding region was cloned in the modified pPCV812 binary plasmid(Pfeiffer et

560 al., 2009) between the *35S* promoter and the *YFP* gene via *Bam*HI (5') and *Sma*I (3')

561 sites, resulting in 35S::CCA1-YFP. Next, the *35S* promoter was replaced by the *CCA1*

562 promoter fragment via *Eco*RI (5') and *Bam*HI (3') sites, resulting in CCA1::CCA1-

563 YFP. The cloned *CCA1* promoter fragment was 862 bp in length and contained the

564 full 5' -untranslated region, but not the ATG.

565

566 **Plant growth material.** The CCA1::CCA1-YFP construct was transformed in *cca1-*

567 *11* (Ws) mutant background (Hall et al., 2003). Homozygous T3 generations of

568 several independent transgenic lines were checked for complementation via delayed

569 fluorescence (Gould et al., 2009) (Figure 1-figure supplement 1b, c). The

570 CCA1::CCA1-YFP expressing line showing full complementation was then re-

571 transformed with *35S*::H2B-RFP which was used for tracking purposes during

572 analysis (Federici et al., 2012). The CCA1:LUC and PRR9:LUC lines used are in the

573 Col-0 background and were built as part of the ROBuST project.

23

574

575   *Arabidopsis* seed were surface sterilised and suspended in 0.1% top agar and placed

576   in 4 °C for 2 days. After sowing, seeds were grown inside of growth incubators

577   (Sanyo MLR-352) under 12:12 LD cycles in 80 umol m^2 s^{-1} cool white light at 22 °C

578   for entrainment. Henceforth, these conditions are referred to as entrainment

579   conditions.

580

581   **Luciferase and delayed fluorescence bulk imaging.** 10-20 seed were sown onto

582   Murashige and Skoog (MS) 2% agar in clear 96 well microtitre plates with at least 8

583   wells per line. A second clear microtitre plate was placed on top of the plate

584   containing the seed to increase well height. These were then sealed using porous tape

585   (Micropore). Seedlings were grown for 9 days under entrainment conditions and

586   transferred to experimental conditions on dawn of the 10th day. For luciferase

587   experiments, on the 9th day seedlings were sprayed with a 5 mM luciferin solution in

588   0.001% Triton x-100 before transfer to experimental conditions on dawn of the 10th

589   day.

590

591   Imaging was carried out in Sanyo temperature controlled cabinets (MIR-553 or MIR-

592   154) at 22 °C and under an equal mix of red and blue LEDs (40 μmol m^{-2} sec^{-1} total).

593   Seedlings were imaged using an ORCA-II-BT (Hamamatsu Photonics, Japan) or

594   LUMO CCD camera (QImaging, Canada). Experiments were run over several days

595   with images being taken every hour as described previously (Gould et al., 2013;

596   Litthauer, Battle, Lawson, & Jones, 2015). Image analysis was carried out using

597   Imaris (Bitplane, Switzerland) or ImageJ (NIH, USA).

598

599 **Luciferase macro imaging.** Seedlings were sown in a row of eight seedlings on 2%

600 agar media supplemented with MS media. Seedlings were grown upright for four days

601 under entrainment conditions. Imaging commenced on dawn of the fifth day. Imaging

602 was performed inside of Sanyo plant growth incubators at 22 °C under an equal mix

603 of red and blue light emitting diodes (40 μmol m^{-2} sec^{-1} total). Seedlings were imaged

604 upright using a LUMO CCD camera (QImaging, Canada). Experiments were run over

605 several days with images being taken every 90 minutes.

606

607 **Confocal microscopy.** For confocal experiments seed were sown directly onto glass

608 bottom dishes (Greiner, Austria) in an array format. Once dry, the seed were covered

609 with 5 ml MS 2% agar media in absence of sucrose. Once set, dishes were sealed with

610 porous tape (Micropore) and grown upright under entrainment conditions for 4 days.

611 After 4 days plates were ready for imaging.

612

613 The microscopy pipeline is outlined in Figure 1-figure supplement 2. Up to 18

614 seedlings were grown in an array format on glass bottom dishes. At dawn on the 4th

615 day of growth the dishes were fixed into the confocal temperature controlled stage (22

616 °C) using the dish manifold. To maintain correct light conditions (30 μmol m^{-2} s^{-2}

617 constant blue light) a custom-made light emitting diode (LED) rig was used. Growth

618 conditions allowed slow growth during the movie, which enabled easier tracking of

619 single cells. A Zeiss 710 (Zeiss, Germany) inverted confocal microscope with a

620 40x/1.2 water corrected oil objective was used for all imaging. YFP and RFP

621 excitation was produced using a 514 nm laser and a main beamsplitter (MBS)

622 458/514. To reduce problems with auto-fluorescence and improve signal to noise ratio

623 a lambda scan was carried using a ChS PMT and filters 492-658. Brightfield (BF)

25

624   used a ChD PMT. Imaging was carried out using a 0.6 zoom to increase field of view.

625   A motorised stage was used to allow multiple positions to be imaged across the plant

626   per experimental run. The diameter of nuclei in our seedlings ranges in size from 6

627   μm (root tip) to 15 μm (hypocotyl). A resolution of 2 μm in the z dimension was

628   chosen to allow the capture of several slices through each nucleus. Data was auto

629   saved during imaging with data split into files by position imaged.

630

631   **Processing confocal images.** Firstly blank images created by time-lapse being

632   terminated early were removed in ImageJ. Also with ImageJ, lambda scans produced

633   during confocal imaging were split into YFP (511 to 547 nm), RFP (586 to 625 nm)

634   and brightfield (BF) spectrums and then reduced in dimensionality to give one

635   channel for each wavelength. Data was then saved as OME TIFF, writing each time

636   point as a separate file. Once processed all the data was loaded into Imaris (Bitplane,

637   Switzerland) and merged to produce one file containing YFP, RFP and BF. A median

638   filter size 3x3x1 was then applied across all of the data. Detection of YFP/RFP

639   expressing cells was carried out using the spot detection feature and tracking of spots

640   over time was carried out using an autoregressive motion model using an estimated

641   cell x,y diameter of 6-10 μm. Data was then exported in excel format for further

642   analysis. Details are provided in the subsequent section. Quality control checks were

643   carried out at multiple points (see Figure 1-figure supplement 2). The first quality

644   check was made to ensure that the seedling remained in the focal plane during the

645   course of the experiment. If not, the dataset was not carried forward for further

646   analysis. The second check was to make sure that all processing has occurred

647   correctly. The third check was carried out to correct any errors in tracking cells across

648   the time-lapse data. The fourth check used the videos to more closely monitor the data

26

649   for anything that looked problematic. The final check used the graphs to identify any

650   problems that may have occurred during the whole single cell pipeline. If the laser

651   power was not found to be stable during the course of the imaging the dataset was not

652   carried forward for further analysis.

653

654   **Single cell data processing.** Period analysis was carried out in BioDare, an online

655   system for data sharing and analysis (Costa et al., 2013; Moore, Zielinski, & Millar,

656   2014). Since most of the period analysis methods in BioDare require evenly spaced

657   time series, the data was first interpolated (using MATLAB's (MathWorks, U.K.)

658   interp1 function and spacing of 1h). Period estimates were obtained by three different

659   methods: Spectrum Resampling (Costa et al., 2013), FFT-NLLS (Johnson & Frasier,

660   1985; Straume, Frasier-Cadoret, & Johnson, 2002) and mFourFit (Edwards et al.,

661   2010). Cells were classed as rhythmic only if each method identified them as

662   rhythmic (i.e. BioDare did not ask to ignore them), their goodness of fit was below 1

663   for FFT-NLLS and mFourfit or 0.9 for Spectrum Resampling and all estimates

664   obtained by different methods were within 2.5h of each other. In Fig. 3, Figure 2 –

665   supplement 1 and 2, the FFT-NLLS period estimates are shown. Period variability

666   within and between cells was calculated as described previously (Kellogg & Tay,

667   2015).

668

669   Since some of the sections imaged overlap (e.g. Figure 2f; Figure 3a; Figure 2-figure

670   supplement 1c, 2c), in order to not count cells multiple times, some of the cells were

671   removed. This was done in the following manner: if there was an area of overlap in

672   multiple sections, only cells belonging to the sections with lower x and y positions

673   were kept, e.g. in Figure 3a, any cells in the upper hypocotyl section that also belong

27

674 spatially to the lower hypocotyl section, were removed from subsequent analysis. In

675 the repeat WT experiment the root tip section imaged encompasses a longer section of

676 the root (Figure 2-figure supplement 1c). Hence, in order to make the analysis

677 comparable to WT (Figure 3), we split the root tip section for further analysis. We

678 considered the root tip cells of the repeat to be only those less than approximately

679 0.66 mm from the actual tip, while the rest of them were classed as 'Root up from tip'

680 (Figure 2-figure supplement 1a, b).

681

682 In the case of analysis at tissue level, where multiple sections had to be pooled for

683 analysis (e.g. Figure 1g, h and Figure 1-figure supplement 3, 4, 5), since different

684 sections were imaged at different times, before any further statistics were done, all the

685 data was interpolated at the times where measurements across any section were made.

686

687 For analysis of amplitudes, peak and trough times for the individual cells (Figure 2a,

688 f, g, and Figure 2-figure supplement 1a, e, f; Figure 2-figure supplement 2a, e, f) were

689 identified using the findpeaks function in MATLAB. This was done on linearly

690 detrended data. In case of the WT data (Figure 2), since the data is sampled more

691 frequently (every 1.1h vs. 3h in WT repeat and CCA1-long line), the data is noisier,

692 hence a smoothing filter (robust local regression using weighted linear least squares

693 and a 2nd degree polynomial model) was also applied after linear detrending.

694 Amplitudes of traces were calculated as a mean of all trough to peak and peak to

695 trough amplitudes.

696

697 **Luciferase space-time analysis.** To facilitate analysis, individual seedlings were

698 manually cropped into individual time stacks using ImageJ. From these image stacks

28

699   a rectangular region of interest (ROI) containing the full length of the root and as

700   much length of the hypocotyl as possible, whilst still excluding the cotyledons, was

701   defined. Custom developed MATLAB scripts were used to extract luminescence data

702   for each pixel in the ROI, giving time series for each pixel. After inspection of the

703   images and the time series, some features were identified and the following measures

704   applied to address them:

705

706   I.   Occasionally the cotyledon of the seedling or of a neighboring seedling

707   protrudes into the ROI. At this stage the ROI was checked for pixels of

708   overlapping seedlings and these regions were manually removed from the

709   affected frames.

710

711   II.   Inside of the ROI the hypocotyl and root are surrounded by peripheral

712   background pixels. The root and hypocotyl were segmented from the

713   background using the mean of the grey levels as the threshold. The algorithm

714   was applied to each image in the stack individually.

715

716   III.   Commonly supposed to be from solar cosmic rays, pixel spikes in intensity

717   values occur sporadically in images. A 3-by-3 pixel median filter is applied to

718   each image to remove these spikes.

719

720   IV.   The luminescence signal strength in a single seedling is weak and therefore

721   the signal to noise ratio relatively low. A third order Butterworth filter was

722   applied to pixel time series to remove high frequency noise. Time series were

723   filtered using MATLAB's filtfilt.m function, which performs in the forward

724 and reverse direction to avoid phase distortion. A cut off frequency of 15% of

725 the Nyquist frequency was identified as a best fit to our data.

726

727 V. In all experiments we observed dampening of the signal over time. Time series

728 were therefore amplitude de-trended to better visualise spatial patterns. Time

729 series were de-trended using the algorithms developed for the mFourfit toolkit

730 (Edwards et al., 2010).

731

732 To visualise spatial patterns across the length of the root, space-time plots of the root

733 luminescence were created (Fig. 3i, Figure 3-figure supplement 1). To do this we take

734 the maximum signal intensity across one pixel wide longitudinal sections of the root

735 for each image and assign this value to position m,n of the space time plot, where m is

736 the image number and n the longitudinal section. The space-time plots presented

737 include 10 pixels of the hypocotyl. The mean luminescence is normalised so that the

738 peak expression of each longitudinal section (n) is 1.

739

740 **Model simulation.** In Figure 1a we simulate an existing deterministic model of the

741 clock (Pokhilko et al., 2012). The model was run for 168h from introduction into

742 constant light conditions and *LHY/CCA1* mRNA is reported (in the model *CCA1* and

743 *LHY* are treated as a single component (Pokhilko et al., 2012)).

744

745 In Figure 2, we simulated a stochastic model of an existing circadian clock model

746 (Guerriero et al., 2012; Pokhilko et al., 2012). In Guerriero et al, the model is scaled

747 by the parameter Ω, so that a molecule count close to Ω is obtained. For detailed

748 description of the scaling, the reader can refer to this paper. Comparison of the model

749   simulated for different Ω values to the previously published data indicates that the

750   model molecule count of a few hundred cells (i.e. Ω) is a good prediction of the actual

751   molecule count (Guerriero et al., 2012). Here we have taken the same circadian clock

752   model and simulated it for various values of Ω. Model equations scaled for the Ω

753   factor are given in (Guerriero et al., 2012). The model was simulated for 200h from

754   introduction into constant light conditions and 100 simulation runs (proxy for 100

755   cells) were performed. The stochastic simulations were performed using the Gillespie

756   algorithm (Gillespie, 1977). For each simulation, further analysis of amplitudes and

757   period was done after the simulated data was interpolated at 2h intervals and then

758   only for the simulated data from 28h to 168h in LL, in order to be closely comparable

759   to the time interval of the original single cell data (Figure 1d). The Gillespie

760   algorithm was written in MATLAB and the amplitudes and periods of the simulations

761   were extracted using the MATLAB findpeaks function. Periods were calculated as a

762   mean difference of peak-to-peak intervals. Amplitudes were calculated as a mean of

763   all trough to peak and peak to trough amplitudes.

764

765   **Synchronisation analysis.**

766   For a set of individual cells, the inter-cellular synchrony was analysed. First, one cell

767   was selected as a centroid of the synchronization analysis. Then, its neighboring cells,

768   defined as those located within its sphere (radius *r*), were extracted. From CCA1-YFP

769   expression signal, phase of the *j*-th neighboring cell (*j=1,2..,N*) was computed as

770   (Pikovsky *et al.*, 2003)

$$\theta_j(t) = 2\pi\,k + \frac{t\text{-}t_k}{t_{k+1}\text{-}t_k}\times 2\pi.$$

771   Here, the *k*-th peak time t_k of the bioluminescence signal was detected by a cosine

772   fitting method (coefficient of determination larger than 0.7) using the estimated

31

773   period τ_i. Then for each time point, the order parameter $R(t)$ (Kuramoto, 1984) was

774   obtained as

$$R(t)\,e^{\Theta} = \frac{1}{N}\sum_{j=1}^{N} e^{-i\theta_j(t)}$$

775   The order parameter ($0<R<1$) becomes unity for completely synchronized cells

776   ($\theta_1=\theta_2=..=\theta_N$), whereas it becomes zero for non-synchronised cells. Figure 3-figure

777   supplement 2 shows the results of synchronization analysis for root tip (**a**), lower root

778   (**b**), upper root (**c**), lower hypocotyl (**d**), upper hypocotyl (**e**), and cotyledon (**f**). For

779   each section, a total of n curves were drawn by selecting individual cells as the

780   centroids (root tip, $n = 242$; lower root, $n = 83$; upper root, $n = 46$; lower hypocotyl, n

781    $= 114$; upper hypocotyl, $n = 53$; cotyledon, $n = 103$). By linear regression analysis of

782   each curve, the slope of the order parameter against time was computed, where a

783   positive slope implies that the level of synchrony increases in time due to cell-to-cell

784   interactions. Figure 3-figure supplement 2h shows the dependence of the slope value

785   on cell density ($\rho=N/(4/3)\pi r^3$). Positive slopes are mostly found in the root tip (Figure

786   3-figure supplement 2g), with a high correlation to the cell density.

787

788   Next, the coupling strength was estimated for each synchronization curve $\{ R(t) \}$.

789   Our approach is based upon a simplified version of the technique developed for

790   weakly interacting mammalian circadian cells (Rougemont & Naef, 2007). As a

791   model for the neighboring cells, we consider a set of coupled phase oscillators

$$\frac{d\theta_j}{dt} = \omega_j + \frac{K}{N}\sum_{k=1}^{N}\sin(\theta_k - \theta_j)$$

792   Assuming that the period τ_j estimated from the j-th cellular trace is not strongly

793   affected by the other cells (Rougemont & Naef, 2007), the natural angular frequency

794   was set as $\omega_j=2\pi/\tau_j$ for each oscillator. Given an initial condition $\theta_j(0)$ extracted from

795   the cellular traces, the phase oscillator model was simulated (Euler method with time

796   step 0.1 h). Accordingly, the time evolution of the order parameter $R(t)$ could be

797   obtained. The coupling strength, which was initially set as $K=0.002$, is constant for

798   each simulation. Staring from the minimum level of coupling, the coupling strength

799   was slowly increased so that the phase oscillators are eventually mutually

800   synchronized and the corresponding slope value increases monotonously. At the point

801   when the slope value exceeds the one obtained from the experiment, the

802   corresponding value of K provides the coupling estimate for the experimental data.

803   Figure 3-figure supplement 2i shows the results. Stronger coupling was estimated for

804   densely populated areas, implying that the cell-to-cell interactions are strengthened

805   when cells are closely located to each other.

806

807   To examine the dependence of the present analysis on the synchrony measure used,

808   the synchronization index (Garcia-Ojalvo, Elowitz, Strogatz, 2004) was utilized in

809   place of the order parameter. The synchronization index has the advantage that the

810   noise-sensitive procedure of phase extraction from the cellular traces is not required,

811   since it can be computed directly from the measured signals. For N cellular traces {

812      $x_j(t) : j=1,2,..,N$ }, the averaged signal $M(t) = (1/N) \sum_j x_j(t)$ is computed. Then the

813   synchronization index is given by

$$R = \frac{\langle M^2 \rangle - \langle M \rangle^2}{(1/N) \sum_j^N \{ \langle x_j^2 \rangle - \langle x_j \rangle^2 \}},$$

814   where <> denotes time average. In a synchronized cellular state, the averaged signal

815   gives rise to a pronounced amplitude, resulting in $R=1$. The fully desynchronized

816   cellular state, on the other hand, results in $R=0$. To see the time evolution of the level

817   of synchrony, the synchronization index $R(t)$ at time t was computed for windowed

818   time traces of $\{ x_j(s) : t\text{-}12 < s < t\text{+}12 \}$ (window: 24h). Figure 3-figure supplement 3

819   shows the analysis results based on the synchronization index. The panels are ordered

820   in correspondence with those of Figure 3-figure supplement 2. Positive slopes are

821   again found in the root tip, implying that the level of synchrony increases in time due

822   to cell-cell interactions. The results are therefore consistent with the ones obtained by

823   the order parameter.

824

825   To examine the dependence of the synchronization analysis on the particular

826   experimental data set used, the order parameters were computed for the CCA1-long

827   line. As shown in Figure 3-figure supplement 4, the slope of the order parameter for

828   the CCA1-long line experiment is again well correlated with the cell density, where

829   highly dense cells are located in the root tip. Although the time resolution was three

830   times lower in this experiment, the same tendency was observed. The WT repeat

831   experiment (Figure 2-figure supplement 1) was not analysed, as the timeseries was

832   too short and time resolution was too low to enable accurate synchronization analysis.

833

834   **Phase oscillator model.** We constructed a model where we describe the dynamics of

835   the CCA1::CCA1-YFP in each cell by a simple Kuramoto phase oscillator. For every

836   cell at a position (m,n) in the plant (when viewed in 2D with m denoting position in

837   the horizontal direction and n denoting position in the vertical direction) the phase of

838   the oscillator $\theta^{(m,n)}$ changes in time (t) so that

839    $\frac{d\theta^{(m,n)}}{dt} = \omega^{(m,n)} + K \sum_{\langle p.q \rangle} \sin (\theta^{(p,q)} - \theta^{(m,n)}).$

840   Here $\omega^{(m,n)}$ describes the intrinsic frequency of the oscillator and the second term

841   describes the oscillator's dependence on the coupling to the nearest neighbours (i.e.

842   cells in positions (p,q) where $p=m\text{-}1,..,m\text{+}1$ and $q=n\text{-}1, ...,n\text{+}1$) with K as the coupling

34

843   constant. The bioluminescence of each cell is then taken to be

844     $B^{(m,n)}(t) = \cos\left(\theta^{(m,n)}(t)\right) + 1$. Cells in the plant conform to a template that is

845   taken to be a symmetric shape, and resembles the shape of a seedling. The total

846   bioluminescence across each vertical section (n) of the plant is taken to be the sum of

847   the bioluminescence of all cells along that section i.e., $B_{tot}^n(t) = \sum_{m=1}^{Nw} B^{(m,n)}(t)$

848   where the width of the plant counts Nw number of cells. The space-time plot shown in

849   Figure 3k shows the total luminescence normalized so that the peak expression of

850   each vertical section is 1.

851

852   In the model we assume that the cells in the three sections (the cotyledon/hypocotyl,

853   the root and the root tip) have different intrinsic periods, with the cells in the

854   cotyledon and hypocotyl having period of 24h, those in the root having the period of

855   around 25.55h and the ones in the root tip a period of 22.67h. These overall match the

856   qualitative period differences seen across the different plant sections. In all

857   simulations the coupling constant K is arbitrarily set to 1. The ODEs are solved using

858   the Euler method.